Post-Print

This is the accepted version of:

The final publication is available at https://doi.org/10.4050/JAHS.63.032007

Access to the published version may require subscription.

When citing this work, cite the original published paper.

Permanent link to this version
http://hdl.handle.net/11311/1055709

Investigation of the Rotor-Obstacle Aerodynamic Interaction in

Hovering Flight

Daniele Zagaglia[*]

Post-Doc Research Fellow

Politecnico di Milano

Dipartimento di Scienze e Tecnologie Aerospaziali

Via La Masa 34, 20156 Milano, Italy

Michea Giuni

Research Assistant

University of Glasgow

Aerospace Sciences Division, School of Engineering

James Watt Building South, Glasgow G12 8QQ, UK

Richard B. Green

Senior Lecturer

University of Glasgow

Aerospace Sciences Division, School of Engineering

James Watt Building South, Glasgow G12 8QQ, UK

[*] Corresponding author: daniele.zagaglia@polimi.it, Tel. +39 0223998070

Abstract

In this paper a comprehensive experimental survey of the aerodynamic interaction of a hovering rotor in the proximity of a ground obstacle is described, taking advantage of multiple experimental techniques. Load measurements on the rotor were carried out in order to assess the change in the rotor performance for different positions with respect to the cubic obstacle, thus simulating a set of possible hovering flight conditions around the obstacle. Laser Doppler Anemometry (LDA) measurements of the rotor inflow were used in order to investigate how the aerodynamic interaction affected the rotor performance. Stereoscopic Particle Image Velocimetry (SPIV) measurements in the region between the rotor and the obstacle were carried out in order to gain a better insight of the interacting flow field. The investigation showed two main regions of interest. The first region is the one above the edge of the obstacle, where the rotor experiences a gradual ground effect as it is positioned over the obstacle. The second region, probably of more interest, is the one just beside the obstacle where a recirculation region between the rotor and the obstacle develops, causing both a significant reduction in the thrust augmentation experienced in unobstructed hover in ground effect and significant pitching and rolling moments, due to the non symmetrical inflow pattern on the rotor.

Nomenclature

Symbols

A rotor disk area, πR^2

c Blade chord

c_∞ Asymptotic speed of sound

c_{Mx}, c_{My} Rotor in-plane moment coefficients, $M_x/(\rho V_{TIP}^2 AR)$

c_P Rotor power coefficient, $Q\Omega/(\rho V_{TIP}^3 A)$

c_Q Rotor torque coefficient, $Q/(\rho V_{TIP}^2 AR)$

c_T Rotor thrust coefficient, $T/(\rho V_{TIP}^2 A)$

FM Figure of Merit, $C_T^{3/2}/(C_Q\sqrt{2})$

M PIV optical magnification factor

M_{TIP} Mach number at Blade tip, V_{TIP}/c_∞

Q Rotor torque

R Rotor radius

Re_{TIP} Reynolds number at Blade tip, $V_{TIP}c/\nu$

T Rotor thrust

V_{IND} Hover induced velocity according to Momentum Theory, $V_{TIP}\sqrt{c_{T,OGE}/2}$

V_{TIP} Blade tip velocity, ΩR

V_z Measured normal induced velocity

(X, Y, Z) Absolute reference System

(x, y, z) Rotor reference System

Δt Laser pulse delay time

ν Fluid kinematic viscosity

ϵ_{c_T} Uncertainty on the Thrust coefficient

ϵ_u Uncertainty on the PIV velocity field, in-plane velocity components

$\epsilon_{u,op}$ Uncertainty on the PIV velocity field, out-of-plane velocity components

θ Half camera separation angle

Ω Rotational frequency of the rotor

Acronyms

AG22 GARTEUR Action Group 22

CIRA Centro Italiano Ricerche Aerospaziali, Italian Aerospace Centre

DI Dynamic Interface

DLR Deutsches Zentrum fur Luft- und Raumfahrt, German Aerospace Centre

GARTEUR Group for Aeronautical Research and Technology in EURope

IHST International Helicopter Safety Team

JHSAT Joint Helicopter Safety Analysis Team

LDA Laser Doppler Anemometry

NLR   Nederlands Lucht-en Ruimtevaartcentrum, Dutch Aerospace Centre

OGE   Out of Ground Effect

ONERA   Office National d'Etudes et de Recherches Aerospatiales,French Aerospace Centre

PIV   Particle Image Velocimetry

RPM   Revolutions Per Minute

Introduction

The helicopter is a very versatile flying machine which is often required to operate within confined areas, owing to its ability to hover and fly under control at very low-speed . These challenging operations areas typically comprise naval environments, e.g. a landing manoeuvre on a helicopter carrier, and rescue operations in confined areas and urban environments where the helicopter interacts with the surrounding buildings.

The aerodynamic interaction between the rotor-induced wake and surrounding obstacles, such as buildings and mountain walls, typically generates, on the one hand, a degradation of the helicopter performance and high compensatory workload for the pilot (Ref. 1), and on the other hand unsteady forces which can stress the structure of the surrounding obstacles. The danger intrinsic to these flight conditions is evident in the accident database of Ref. 2, collected by the Joint Helicopter Safety Analysis Team (JHSAT) for the International Helicopter Safety Team (IHST). The gathered database analyses 523 helicopter accidents that occurred in the United States of America in 2000, 2001 and 2006, sorting them in terms of flight phase, occurrence category and motivation. This study highlighted that most of the helicopter accidents (61.4 %) occur during take-off and landing, hence potentially in the presence of ground obstacles. In particular, 41% of the total number of accidents were attributed to pilot performance management issues, i.e. the fact that the pilot was not capable of accounting for the change in the helicopter performance due to external perturbations.

The number of experimental studies regarding the rotor interaction with simplified geometries (i.e. semi-infinite vertical walls, parallelepipeds, etc.) is unexpectedly small in comparison to those comprising more complex geometries (e.g. ship superstructures). Among these, Timm in Ref. 3 was the first to

observe the flow recirculation induced by the interaction between the rotor and obstacle through flow visualisation. Iboshi et al. investigated in Ref. 4 the ground effect of a fully articulated rotor in ground effect above a confined area between two vertical walls, finding that the re-circulatory flow upward along the wall causes both the steady and vibratory torque coefficients to increase. The effect is either a downwash or up-wash based on the combinations of the wall height, the space between walls, and the rotor height.

For the helicopter interaction with more complex geometries, the Dynamic Interface problem (Ref. 5), i.e. the launch and recovery of flight vehicles, primarily rotorcraft, onto ships, is probably the most investigated configuration from both the experimental and numerical point of view. On this topic, one of the first experimental works was produced by Zan in Ref. 6, where he presented the experimental measurements of time-averaged rotor thrust coefficients for a rotor immersed in the airwake of the Canadian Patrol Frigate ship. Further studies allowed to investigate also the unsteady loads on the fuselage immersed in the ship wake (Lee and Zan, Ref. 7) and the full configuration comprising rotor and fuselage (Lee and Zan Ref. 8). The experimental investigations found in the literature do not only focus on the change in the rotor performance, but they also rely on other kind of flow measurements. As an example, Quinliven at al. (Ref. 9) investigated the inflow region and the wake of a rotor in proximity of a building model, highlighting the effect of the flow-recirculation that occurs when the rotor is close to the building. A different measurement technique was adopted by Rajagopalan et al in Ref. 10, where Particle Image Velocimetry (PIV) was used to acquire 3-component velocity field measurements of the combined wake of a tandem-rotor helicopter and a ship. PIV was also used by Konuş and Savaş in Ref. 11 to investigate the rotor wake in close proximity to vertical walls, and by Nacakli and Landman in Ref. 12 to investigate the recirculation region between a rotor and the vertical wall of a ship deck.

Despite the presence of several numerical and experimental works, a systematic study of these aerodynamic phenomena is lacking. The GARTEUR Action Group 22 *"Forces on Obstacles in Rotor Wake"*, comprising several universities (Politecnico di Milano, University of Glasgow, National Technical university of Athens) and research institutes (CIRA, DLR, ONERA, NLR), originated with the idea of promoting activities which could contribute to a better understanding of these phenomena. In this framework, the production of an experimental database was carried out initially at Politecnico di Milano (Ref. 13), analysing the case of a model helicopter with fuselage interacting with a cuboid obstacle. Following this,

an extended database comprising several measurement points and experimental techniques was produced at University of Glasgow to gain additional insight into the interacting flow, which is the subject of the present paper.

As previously stated a systematic study of the aerodynamic phenomena involved is still lacking. Moreover the past investigations usually either rely on just one measurement technique or they usually involve quite specific geometries (e.g. ships). The idea behind the present work is thus to experimentally investigate this problem, and simplify the obstacle geometry to a well-defined cubic shape in order to reveal the key fluid-dynamic mechanisms that occur when a rotor is hovering in its proximity.

The variation of the rotor performance was monitored by means of a six-component load cell. Laser Doppler Anemometry (LDA) measurements of the rotor inflow were used in order to investigate how the aerodynamic interaction affected the rotor performance. Finally Stereoscopic Particle Image Velocimetry (SPIV) measurements in the region between the rotor and the obstacle were carried out in order to have a better insight of the interacting flow field.

The Experimental Campaign

The Experimental Setup

The experimental campaign was conducted at University of Glasgow. It used two different rotor rigs, each rotor interacting with a cube shaped obstacle whose size was the same as the rotor diameter. The main features of the two rotor rigs are reported in Table 1. The collective blade pitch angle was fixed to $8°$, whereas the lateral and longitudinal cyclic pitch were set to zero. The prescribed rotational speed was maintained during all the tests by means of a brush-less motor and was monitored from the motor speed feedback signal and with a stroboscope. No appreciable speed fluctuation (less than 1 RPM) was recorded during the tests. The two rotor rigs were used for different kind of measurements. In particular the Large rotor rig was used for the load measurements and the inflow LDA measurements, whereas the Small rotor rig was used to investigate the flow-field by means of Stereoscopic Particle Image Velocimetry (PIV). The operating conditions were such that the blade solidity and blade tip Mach number were the same for both the Large and Small rotor setups.

Since the main goal of the small rotor rig was to perform a time averaged flow visualisation of the interaction phenomena, the most important common parameters for the two rotor rigs were the solidity and the thrust coefficient, which were indeed sufficiently similar, as seen in Table 1. For a time-dependent description of the rotor wake the number of blades would obviously greatly influence the dynamics of the trailed vortices, but this was beyond the goals of the paper.

Both the Large and Small rotor rigs were characterised by a non-articulated, rigid, rotor hub, with no flap or lag blade motion which are quite difficult to monitor on a small-scale model. In this way, the rotor geometry was *a priori* known and well-defined, while the general wake features were still representative of those of a real rotor. Owing to the presence of the flap hinges, a real rotor would experience less intense in-plane moment than those experienced by the fixed rotors, however the measured in-plane moments can still give a reasonable indication of the strength of the interaction for the different rotor positions and the order of magnitude of the effects that in real flight would have to be compensated by a pilot.

In addition, the choice of carrying out the experiments at fixed collective pitch prevents a sensitivity analysis of the disk-loading, which represents an important parameter for the characterisation of the wake strength. However this is beyond the purpose of the present work, to reveal the key fluid-dynamic mechanisms that occur in this kind of interaction, even though it is recommended for future investigations.

Two different reference systems are defined, as depicted in Fig. 1. The global reference system (X, Y, Z) defines the position of the rotor hub centre with respect to the obstacle, whereas the rotor reference system (x, y, z) coincides with the load-cell axes. The origin of the absolute (X, Y, Z) coordinate system is fixed and it is placed on the floor, at the obstacle mid-span, so that the X-coordinate represents the distance of the rotor centre from the obstacle, the Y-coordinate represents the distance of the rotor centre from symmetry plane and the Z-coordinate represents the height of the rotor centre from the ground.

The Large test rig was placed in a large laboratory space with an even, flat ground extending to a 5 m radius away from the rotor centre line, corresponding to 5 rotor diameters. The Large rotor rig was instrumented with a 6-component load cell which allowed the measurements of the forces and moments generated by the rotor. The load cell was an AMTI MC36, with amplifier set at a very high sensitivity so that it would respond to the forces and moments. The nominal accuracy of the load cell was 0.25% of the

full-scale output, corresponding approximately to 0.5% of the measured thrust in Out of Ground Effect condition. The actual load measurements were obtained as the average of 5 runs, each of which was $2.5\ s$ long. The reduced acquisition time was driven by the need to reduce the load-cell thermal drift.

In order to understand how the aerodynamic interaction affected the rotor performance, a measurement of rotor inflow was performed. In classical aerodynamics the in-flow velocity is treated as uniform across the disc and constant with time, but in practice the inflow is non-uniform and additionally unsteady due to the blade passing and wake effects. Inflow should be measured as close to the plane of the disk as possible, and consequently an optical method was preferred, but the requirement for unsteady flow measurement needs to be considered also. The rotor inflow measurements were carried out using a commercially available Dantec 2D FiberFlow two-component Laser Doppler Anemometry (LDA) system. A 112 mm diameter probe of 2 m focal length fitted with a beam expander allowed velocity measurements within a measurement volume ellipsoid of 2.62 mm×0.12 mm×0.12 mm. The probe axis was in the horizontal plane and was rotated by $45°$ such that the LDA sensors responded to both vertical and horizontal velocity, and the inflow was calculated from an axis transformation. In anticipation of elevated turbulence levels in the obstacle flow case and to avoid the velocity-bias effect, the system was set to burst mode with transit (residence) time enabled for calculation of the mean flow velocity, as suggested by Ref. 14 and 15. Seeding was provided by a mineral oil based system that used a peristaltic pump to pump the oil through a heater matrix. The smoke oil had a substrate density $843\ \mathrm{kg/m^3}$ at room temperature, and the seeder unit manufacturer's calibration indicated a particle diameter of $0.2\ to\ 0.3\ \mu\mathrm{m}$ at the recommended heater operation temperature. During LDA operation a typical burst rate of 1000 counts per second (in the root region of the rotor) to 2000 (in the outboard region) was achieved, equivalent to 50 to 100 counts per revolution. Sampling runs were performed to assess convergence for mean and root-mean-square velocity, and subsequently 7500 valid samples were taken at every measurement point, with absolute accuracy of approximately 0.02 m/s corresponding to 0.4% of the maximum inflow velocity. The LDA system was mounted on a 3D traverse system allowing positioning with accuracy of better than 0.1 mm. The LDA measurements were performed along the rotor x and y axes, 4 cm $(4\%D)$ above the rotor plane, as represented in Fig. 2. Every LDA sweep comprised 101 evenly-spaced measurement points along the rotor diameter, allowing a spatial resolution of 10 mm $(1\%D)$. The LDA measurements are defined

in the rotor reference system (x, y, z). Hence, according to this convention, a positive induced velocity points downwards. The LDA results will be shown scaled by the hover induced velocity estimated through momentum theory, i.e. $V_{IND}=V_{TIP}\sqrt{c_{T,OGE}/2}$.

A quantitative flow visualisation survey was then performed to gain an understanding of the structure of the recirculating flow field caused by the interaction of the rotor wake with the obstacle. It was not possible to do this by recording the behaviour of smoke filaments due to diffusion of the smoke, so PIV was used with a view to observing the mean flow. In this case Stereoscopic PIV was used to investigate the flow in the region between the obstacle and the rotor using the Small rotor rig. These measurements were carried out in the University of Glasgow deHavilland closed-return low-speed wind tunnel, which has a 2.66 m wide $\times$ 2.07 m high (8.9 $\times$ 7 rotor diameters) working section that is 5.4 m long. The PIV system used was a commercially available system by LaVision running Davis 8. The wind tunnel was not run during the experiments as the tests were not meant to simulate flow in a cross-wind. The working section was open to the settling chamber on the upstream side and to the first diffuser leg on the downstream side, but was confined by the ground, ceiling and side walls of the working section. The emphasis of the tests is on an evaluation of the structure of the rotor wake flow field due to the close proximity of the obstacle. Ref. 11 used a water tank to observe the effects of vertical walls on a rotor wake evolution, and while the close proximity of the vertical walls dominated the wake development, the free surface and tank floor and sides will have confined the flow in the far field. The relative size of the wind tunnel working section is larger in the current work, and there is no confinement due to the ends of the test chamber. While the test conditions might produce a limited degree of recirculation of the flow in the test chamber, this can be expected to be not significant when compared to the effect of the obstacle at a close range, and the PIV will provide an effective flow visualisation and useful velocity magnitude data.

The digital PIV method deployed was the widely used dual image, cross-correlation technique. Stereoscopic images were acquired by two 4Mpixel Phantom v341 cameras. The seeded flow was illuminated by a Nd:YAG laser capable of 100mJ pulses of 8 ns duration at a maximum repetition rate of 200 Hz, however the sample rate was actually set to 197 Hz in order to prevent phase-locked measurements at $0°$, $120°$ and $240°$ and have a statistically representative database of the different blade phases. The ensemble-averaged measurements over 500 image pairs are presented in this paper, corresponding to an acquisition

over approximately 170 rotor revolutions. The cameras, which were placed on the same or either side of the laser sheet, depending on the orientation of the light sheet, were equipped with Scheimpflug adaptors, an angle separation of 29.6 degrees was used. Calibration was performed using a 3D calibration plate and Davis 8 software. PIV seeding was generated by a PIVTEC Laskin nozzle based system that atomised olive oil to produce a nominal particle diameter less than 1μm according to the manufacturer's documentation. The image pairs were post-processed by means of the Davis 8 software using 32×32 pixels interrogation windows with an overlap factor of 50%. Window shifting was deployed to enhance accuracy and mitigate against peak-locking. The PIV velocity measurements will be shown scaled by the hover induced velocity V_{IND}, as for the LDA measurements.

Three measurement planes were investigated, as depicted in Fig. 3. The first was the the symmetry plane of the problem, i.e $Y/R = 0$. In this PIV configuration, the cameras were placed on either side of the laser sheet. The uncertainty of the velocity measurement was estimated (according to Ref. 16) to be $\epsilon_u = \frac{1}{\sqrt{2}} \frac{0.1}{M \Delta t} = 0.1 \; m/s$ for the in-plane velocity components and $\epsilon_{u,\text{op}} = \frac{1}{\sqrt{2} \tan \theta} \frac{0.1}{M \Delta t} = 0.33 \; m/s$ for the out-of-plane component, assuming a maximum displacement error of 0.1 pixels since a gaussian sub-pixel interpolation algorithm was used. An optical magnification factor of M =3.4161 pixel/mm was obtained through the calibration process, together with a pulse separation time of $\Delta t = 200 \; \mu s$ and $\theta = 14.8°$, corresponding to half of the camera separation angle, as represented in Fig. 3. The other investigated planes were two transverse planes at different distance from the obstacle, namely $X/R = 0.1$ and $X/R = 0.4666$. In this PIV configuration, the cameras were placed on the same side of the laser sheet. The uncertainty of the velocity measurement was estimated to be $\epsilon_u = 0.07 \; m/s$ for the in-plane velocity components and $\epsilon_{u,\text{op}} = 0.23 \; m/s$ for the out-of-plane component, since an optical magnification factor of M =4.85 pixel/mm resulted from the PIV calibration. So-called peak locking effects were not significant due to the flow area being interrogated, the image size, the camera lens f-number and the analysis method deployed (window-shifting and sub-pixel interpolation), as confirmed by the ensemble velocity histograms.

The Test Matrix

The experimental campaign consisted of a set of tests reproducing hovering flight conditions at several rotor positions with respect to a simplified obstacle with a cubic shape. The text matrix for the loads measurements is represented in Fig. 4, where each circle represents the position of the rotor hub centre for that particular test. It consists of several measurement points at the heights of $Z/R = 1, 3/2, 2, 3$ and 4. The measurements were carried out placing the rotor in two different planes: $Y/R = 0$, corresponding to the problem symmetry plane and $Y/R = 1$, corresponding to a plane tangent to the obstacle lateral face.

The loads and moments will be expressed according to the rotor reference system (x, y, z). Hence a positive M_y moment is equivalent to a pitching nose-up moment if a helicopter was facing the wall. Similarly, a positive M_x moment is equivalent to a roll moment that promotes a thrust rotation towards the positive y-coordinate.

The LDA measurements were carried out in a subset of the measurement points of Fig. 4, i.e. those at $Z/R = 3/2$ and 3, due to the maximum and minimum height achievable by the traversing system. The Stereo-PIV measurements were carried out just for the test points at which the rotor was positioned in the symmetry plane, i.e. $Y/R = 0$. In particular the symmetry plane $Y/R = 0$ was investigated for the rotor positions X/R and Z/R varying from $3/2$ to 3, whereas the two transverse planes were acquired just for $X/R = 3/2, Z/R = 2$ and $X/R = 2, Z/R = 2$.

Results and Discussion

In this section the main results of the experimental survey will be presented. The load measurements for the different rotor position are presented in Fig. 6, 7 and Fig. 8, while the LDA inflow measurements along the x and y rotor-axes are presented in Fig. 9 and 10. The PIV measurements in the symmetry plane $Y/R = 0$ are presented in Fig. 11 (in-plane velocity magnitude contours and streamlines), while the transverse planes are presented in Fig. 12 and 13.

A set of load measurements were initially carried out in order to quantify the rotor performance in absence of the obstacle. The rotor was placed as high as possible ($Z/R = 4$) in order to assess the Out-

of-Ground-Effect (OGE) condition. A $c_{T,\mathrm{OGE}}$ of $7.36 \cdot 10^{-3}$ and a $c_{Q,\mathrm{OGE}}$ of $8.75 \cdot 10^{-4}$ were obtained, leading to a Figure of Merit of $FM_{\mathrm{OGE}} = 0.51$, as summed up in Table 2.

All the results for the thrust and power coefficients will be presented from now scaled by their respective OGE values, in order to appreciate their variation from the reference condition, while the moment coefficients c_{Mx} and c_{My} will be presented through their ratio with $c_{Q,\mathrm{OGE}}$, so that they are expressed as fraction of the OGE torque. Although it is well known that the torque and power coefficients are numerically equal, the former denomination will be used when dealing with considerations on the moments generated on the rotor, the latter when dealing with considerations on the rotor efficiency.

The results of the Ground Effect test, positioning the rotor at different height in absence of the obstacle, are shown in Fig. 5. The typical thrust increase, up to 20% of the OGE value, can be seen as the rotor is positioned closer to the ground.

Results, rotor placed in the symmetry plane $Y/R = 0$

Variation of the thrust coefficient with respect to the out-of-ground-effect (OGE) condition is presented in the plots of Fig. 6a, 6b and 8a. The typical thrust increase (up to 20%) due to the ground effect can be observed in both the region over the centre of the obstacle and far from the obstacle, since the relative distance to the closest surface (either the floor or the top of the obstacle) is the same $(1R)$ and the rotor projection lies completely on the obstacle top face. The comparison between the variation of the thrust coefficient above and far from the obstacle is presented in Fig.5, showing that the extent of the finite ground plane necessary to produce IGE performance benefits does not need to be much bigger than the projected area of the rotor. However two main regions where the rotor performance deviates from the nominal behaviour can be observed.

The first region is the one above the edge of the obstacle, where the thrust coefficient decreases as the rotor is positioned outwards, owing to the minority of the rotor lying over the upper surface of the obstacle. This phenomenon can be appreciated also in the inflow profile of Fig. 9a measured by means of the LDA system. In this case a gradual reduction of the inflow velocity is observed going from $X/R = 1$ to $X/R = -1$, as prescribed by the ground effect. However, one would expect this variation to be non-

symmetrical, since only part of the rotor projection lies on the top of the obstacle and thus is affected by the ground effect. However this appears not to be the case since the inflow profiles of Fig. 9a remain approximately symmetrical as the rotor is placed in the different positions above the obstacle. This is also reflected by the fact that the the pitch and roll moments of Fig. 7a and 7c are quite close to zero in the region $-1 < X/R < 1$. An additional interesting moment behaviour can be observed moving the rotor away from the obstacle ($1 < X/R < 3$) at the same heights ($Z/R = 3, 4$), where a positive $y-$moment develops on the rotor, which disappears farther outboard ($X/R > 4$).

The second region, probably of more interest, is the one just beside the obstacle ($1 < X/R < 3$, $1 < Z/R < 3$), where a severe ground effect reduction can be observed (Fig. 6b), since the thrust coefficient drops to a value slightly below the OGE one, even at low heights. This behaviour is caused by the development of a recirculation regime in the region between the rotor and the obstacle. The rotor wake, once deflected by the ground, is deflected again by the obstacle and then re-ingested by the rotor itself. This recirculation region, which is evident in the PIV flow-fields of Fig. 11, causes an increased induced velocity and a consequent loss of thrust, similar to a partial vortex ring state. This effect is deeply dependent on both the rotor height and distance from the obstacle. A maximum thrust loss of 8% with respect to the furthest rotor position at the same height can be observed at $Z/R = 1$ and $3/2$, whereas at $Z/R = 2$ the maximum thrust loss is lower (approximately 4 %). Moreover one can appreciate the fact that the thrust loss is not monotonic when getting closer to the obstacle, but it presents a local minimum at approximately $X/R = 2$. This can be explained looking at Fig. 11, where at $X/R = 2$ (Fig.11d, 11e, 11f) the upwards in-plane velocity close to the front face of the obstacle (the green layer) is higher than in the other cases (approximately of the order of V_{IND}, instead of half of V_{IND}), thus implying a stronger recirculation. In the other cases (further and closer to the obstacle) most of the air flows round the side of the obstacle instead of being redirected upwards. The effects of the obstacle start to be negligible when the rotor is further than 4 radii from the obstacle itself.

Another important feature of this region is the appearance of a strong nose-down pitching moment (up to 30% of the measured torque, Fig. 8g). This is due to the fact that the previously-introduced recirculation region mainly affects the portion of the rotor closer to the obstacle as it is shown in Fig. 9c, where an increased induced velocity can be observed in the left portion of the inflow profile for $X/R = 3/2$.

Consequently, a negative c_{My} moment is generated on the rotor, which is evident in Fig. 7d and 8g for $Z/R = 3/2$ and $Z/R = 2$ close to the obstacle, which is equivalent to a nose-down pitching moment if a helicopter was facing the wall. A rolling moment, even if with a much smaller value with respect to the $y-$moment, develops as well in the region to the side of the obstacle, as can be seen in Fig. 7b and 8e, even if with a much smaller value with respect to the $y-$moment. This behaviour can be explained by the different composition of the horizontal velocity arising from the recirculating cell with the advancing and retreating blade, causing a different loading between the left and right side of the rotor.

With reference to rotor efficiency, quite limited variations of the torque coefficient, and therefore of the power coefficient, were observed among all the rotor positions. These variations were usually inferior to 5% of the OGE value, as it can be appreciated in Fig. 6c, 6d and 8c.

In order to reveal the main features of the flow-field in the symmmetry plane $Y/R = 0$, the in-plane velocity magnitude contours and streamlines are presented in Fig. 11. As we can appreciate, the recirculation region is present in all the cases, even though its morphology is highly case-dependent. At $X/R = 3/2$ (Fig. 11a, 11b, 11c) the rotor slipstream does not impinge on the floor before being deflected towards the obstacle, but impinges directly on the obstacle. This is due to the formation of a counter-rotating (with respect to the main one) recirculation region on the floor. This region is pushed towards the obstacle as the rotor is moved downwards. At $X/R = 2$ (Fig. 11d, 11e, 11f), as already highlighted in the previous paragraphs, the rotor wake impinges on the floor before being deflected by the obstacle and re-ingested by the rotor. The air-layer that goes upwards close to the obstacle is thicker and faster than the other cases, probably indicating a stronger interaction with the rotor (confirmed, as previously stated, by the thrust measurements). Eventually at $X/R = 3$ (Fig. 11g, 11h, 11i) the flow pattern is very similar to a non-disturbed rotor wake in ground effect, suggesting that the interaction in this case is weaker (as the load measurements also confirm).

Two transverse planes at $X/R = 0.1$ (close to the obstacle) and $X/R = 0.466$ (close to the rotor) were also investigated by means of PIV in order to have a deeper insight of the recirculating flow field, for two different rotor positions: $X/R = 3/2$, $Z/R = 2$ (Fig. 12) and $X/R = 2$, $Z/R = 2$ (Fig. 13).

Consider first the plane at $X/R = 0.1$. When the rotor is positioned at $X/R = 3/2$, the rotor wake directly impinges on the lower part of the obstacle, as previously appreciated in flow-field in the symmetry

plane of Fig. 11c. There is also evidence in Fig. 12a, where the upper part of the obstacle is affected by the upwards velocity of the recirculation region, whereas the lower part presents a downwards velocity. This phenomenon is not observed anymore when the rotor is placed further from the building as seen in Fig. 13a, since the rotor wake impinges on the floor before being deflected towards the obstacle. In both cases the out-of plane velocity component is almost null due to the obstacle blockage effect. Part of the rotor wake is not deflected by the obstacle, but it skims its lateral faces as highlighted by the two regions on the side of the building characterised by a higher out-of-plane velocity.

The second transverse PIV measurement plane at $X/R = 0.466$ directly slices the rotor wake, which can be recognised as the negative (blue) high out-of-plane velocity region. However since the position of the measurement plane with respect to the obstacle is the same for the two cases but the rotor position varies, the two slices represent different regions of the rotor wake. In the first case (rotor at $X/R = 3/2$), the plane is closer to the rotor, therefore the wake is sliced in at a higher position (Fig. 13a), whereas in the second case (rotor at $X/R = 2$), the wake has already impacted on the floor and it is going towards the obstacle as can be appreciated in Fig. 13b.

Results, rotor placed out of the symmetry plane, $Y/R = 1$

The effect of placing the rotor at $Y/R = 1$, out of the symmetry plane of the problem, is analysed in this subsection. As in the previous case, two main regions where the rotor performance deviates from the nominal behaviour can be observed: the region above the edge of the obstacle and the one on the side of the obstacle.

In the first region, a gradual ground effect can be observed as the rotor is moved over the obstacle, similarly to the tests at $Y/R = 0$. However the observed ground effect is weaker as can be appreciated in Fig. 6a and 8b, due to the fact that in the innermost postion $X/R = -1$, just half of the rotor projection lies on the upper surface of the obstacle. This is also evident when comparing the LDA inflow measurements of Fig. 9a and 9b: the reduction in the induced velocity is less intense when the rotor is placed at $Y/R = 1$. However, as for $Y/R = 0$, the inflow profiles remain almost symmetrical, leading to very small x and y moments in the region $-1 < X/R < 1$ (Fig. 7a and 7c).

In the second region, the one on the side of the obstacle, the effect of the flow recirculation on the rotor performance becomes less intense with respect to the tests at $Y/R = 1$, according to the fact that only half rotor faces the obstacle. The thrust coefficient reduction is less pronounced as the rotor is placed closer to the obstacle, as can be appreciated in Fig. 6b. Consequently also the $y-$moment generated in this region is less intense (Fig. 8h). However, since just the negative $y-$portion of the rotor (if we consider a helicopter facing the obstacle) is affected by the recirculating flow, a negative $x-$moment is generated on the rotor, as can be appreciated in Fig. 7b. If we imagine a helicopter facing the obstacle, this moment corresponds to a roll moment that promotes a thrust rotation to the left.

Conclusions

In the present paper a comprehensive experimental survey of the aerodynamic interaction between a rotor and a model ground obstacle has been described. The experimental activities, carried out at University of Glasgow, used two rotor rigs and several experimental techniques. Load measurements on the rotor were carried out in order to assess the rotor performance for different rotor positions with respect to the obstacle. Laser Doppler Anemometry (LDA) measurements of the rotor inflow were used in order to see how the aerodynamic interaction affected the rotor performance. Particle Image Velocimetry (PIV) measurements in the region between the rotor and the obstacle were carried out in order to have a better insight of the interacting flow field.

The investigation examined two scenarios of interest to pilots: flying over the object and flying to the side of the object. The first region of interest, corresponding to the first scenario, is the one above the edge of the obstacle, where the rotor experiences a gradual ground effect as it is positioned over the obstacle. In this case also a gradual reduction of the inflow velocity is observed, as prescribed by the ground effect. Since only part of the rotor is over the obstacle, one would expect the inflow to be non-symmetrical. However, results show it is indeed symmetrical, leading to the generation of almost null pitch and roll moments. When the rotor is completely over the obstacle the experienced ground effect is equivalent to the one measured with an infinite surface underneath, showing that the extent of the finite ground plane necessary to produce IGE performance benefits does not to be much bigger than the the projected area of

the rotor.

The second region, probably of more interest, is the one just beside the obstacle where a recirculation region between the rotor and the obstacle develops. Its morphology is deeply dependent on the rotor position. This recirculation region implies a severe thrust loss (up to 8%) with respect to the one without obstacle at the same height, implying that pilots should not plan for IGE augmented performance when landing close to a vertical obstacle, since that augmentation can be lost due to adverse interactions with obstacle itself. This thrust loss has a maximum at approximately 2 radii from the obstacle. Another important feature of this region is the development of strong pitching and rolling moments (up to 30% of the measured torque), due to the non symmetrical inflow pattern on the rotor. When the rotor is positioned out of the symmetry plane of the problem, the effect of the flow recirculation on the rotor performance becomes less intense, owing to the fact that only half rotor faces the obstacle. Consequently also the pitch-moment generated in this region is less intense.

Limited torque variations were observed throughout the testing. The obstacle influence on the rotor appears to be negligible when the rotor is more than 4 radii away from the obstacle.

Acknowledgments

References

[1]Lee, D., Sezer-Uzol, N., Horn, J. F., and Long, L. N., "Simulation of Helicopter Shipboard Launch and Recovery with Time-Accurate Airwakes," *Journal of Aircraft*, Vol. 42, (2), 2005, pp. 448–461, https://doi.org/10.2514/1.6786.

[2]U.S. Joint Helicopter Safety Analysis Team, "The Compendium Report: The U.S. JHSAT Baseline of Helicopter Accident Analysis," Technical Report, International Helicopter Safety Team, 2011, http://www.ihst.org/portals/54/US_JSHAT_Compendium_Report1.pdf.

[3]Timm, G. K., "Obstacle Induced Flow Recirculation," *Journal of the American Helicopter Society*, Vol. 10, (4), 1965, pp. 5–24, https://doi.org/10.4050/JAHS.10.5.

[4]Iboshi, N., Itoga, N., Prasad, J., and Sankar, L. N., "Ground Effect of a Rotor Hovering above a Confined Area," *Frontiers in Aerospace Engineering*, Vol. 3, (1), 2014, pp. 7–16, https://doi.org/10.14355/fae.2014.0301.02.

[5]Zan, S., "On Aerodynamic Modelling and Simulation of the Dynamic Interface," *Proceedings of the Institution of Mechanical Engineers, Part G: Journal of Aerospace Engineering*, Vol. 219, (5), 2005, pp. 393–410, https://doi.org/10.1243/095441005X30315.

[6]Zan, S., "Experimental Determination of Rotor Thrust in a Ship Airwake," *Journal of the American Helicopter Society*, Vol. 47, (2), 2002, pp. 100–108, https://doi.org/10.4050/JAHS.47.100.

[7]Lee, R. G. and Zan, S. J., "Unsteady Aerodynamic Loading on a Helicopter Fuselage in a Ship Airwake," *Journal of the American Helicopter Society*, Vol. 49, (2), 2004, pp. 149–159, https://doi.org/10.4050/JAHS.49.149.

[8]Lee, R. G. and Zan, S. J., "Wind Tunnel Testing of a Helicopter Fuselage and Rotor in a Ship Airwake," *Journal of the American Helicopter Society*, Vol. 50, (4), 2005, pp. 326–337, https://doi.org/10.4050/1.3092869.

[9]Quinliven, T. and Long, K., "Rotor Performance in the Wake of a Large Structure," American Helicopter Society 65th Annual Forum Proceedings, Grapevine, TX, May 2009.

[10]Rajagopalan, G., Niazi, S., Wadcock, A., G.K.Yamauchi, and Silva, M., "Experimental and Computational Study of the Interaction between a Tandem-Rotor Helicopter and a ship," American Helicopter Society 61st Annual Forum Proceedings, Grapevine, TX, June 2005.

[11]Konuş, M. F. and Savaş, Ö., "Rotor Vortex Wake in Close Proximity of Walls in Hover," *Journal of the American Helicopter Society*, Vol. 61, (4), 2016, pp. 1–12, https://doi.org/10.4050/JAHS.61.042003.

[12]Nacakli, Y. and Landman, D., "Helicopter Downwash/Frigate Airwake Interaction Flowfield PIV Surveys in a Low Speed Wind Tunnel," American Helicopter Society 67th Annual Forum Proceedings, Virginia Beach, VA, May 2011.

[13]Gibertini, G., Grassi, D., Parolini, C., Zagaglia, D., and Zanotti, A., "Experimental Investigation on

the Aerodynamic Interaction between a Helicopter and Ground Obstacles," *Proceedings of the Institution of Mechanical Engineers, Part G: Journal of Aerospace Engineering*, Vol. 229, (8), 2015, pp. 1395–1406, https://doi.org/10.1177/0954410014550501.

[14]George, W. K., "Quantitative Measurement with the Burst-Mode Laser Doppler Anemometer," *Experimental thermal and fluid science*, Vol. 1, (1), 1988, pp. 29–40, https://doi.org/10.1016/0894-1777(88)90045-3.

[15]Albrecht, H.-E., Damaschke, N., Borys, M., and Tropea, C., *Laser Doppler and Phase Doppler Measurement Techniques*, Springer Science & Business Media, 2013.

[16]Prasad, A. K., "Stereoscopic Particle Image Velocimetry," *Experiments in fluids*, Vol. 29, (2), 2000, pp. 103–116, https://doi.org/10.1007/s003480000143.

List of Figures

List of Tables

Fig. 1: Global (X, Y, Z) and Rotor (x, y, z) reference systems.

Fig. 2: Position of the LDA measurement points along the rotor x and y axes.
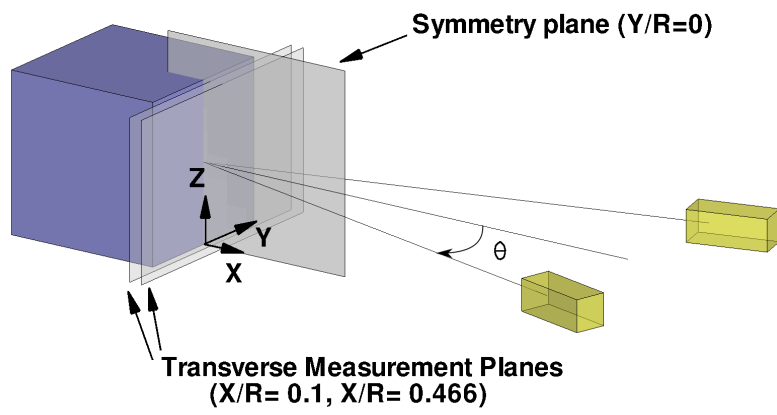
Fig. 3: PIV setup and measurement planes
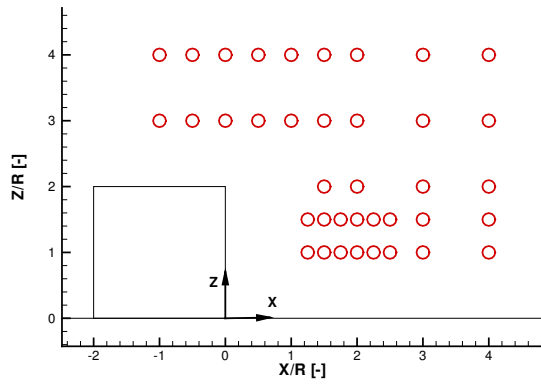
(a) Test Points - Lateral View
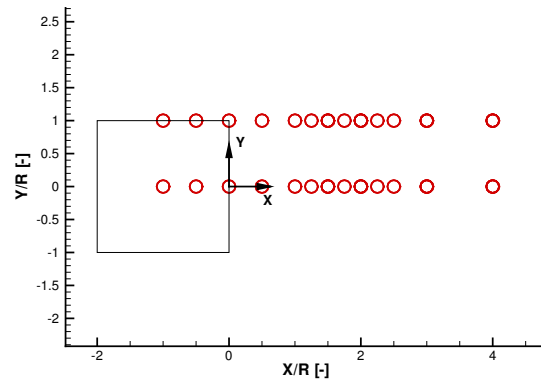
(b) Test Points - Birdseye View

Fig. 4: Test Points. Each circle represents the position of the rotor hub centre for that particular Test Point.
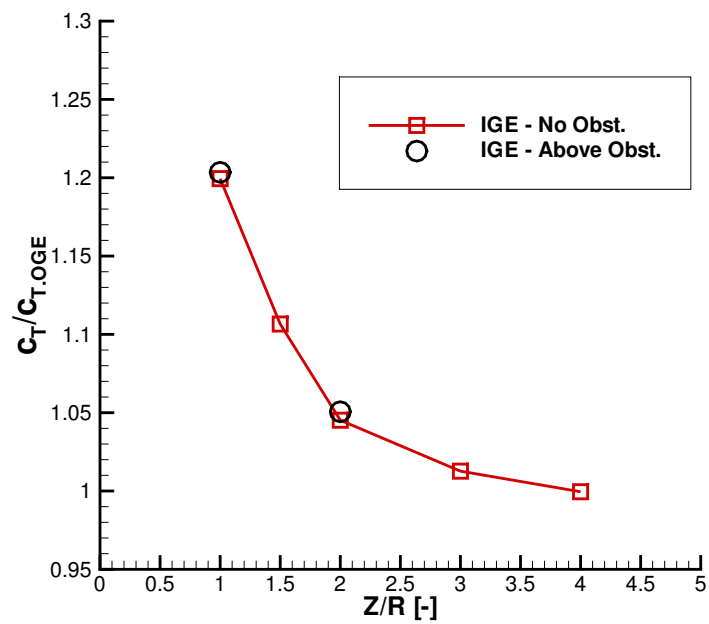
Fig. 5: Ground effect test in absence of the obstacle (red markers) and above the obstacle ($X/R = -1$, black markers). The latter data have a Z/R offset of 2, equal to the obstacle height.
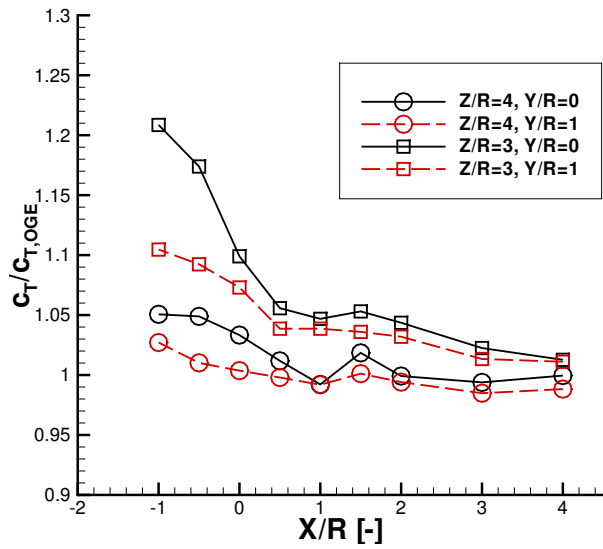
(a) Ratio of thrust coefficient c_T to thrust coefficient OGE, $Z/R = 3, 4$
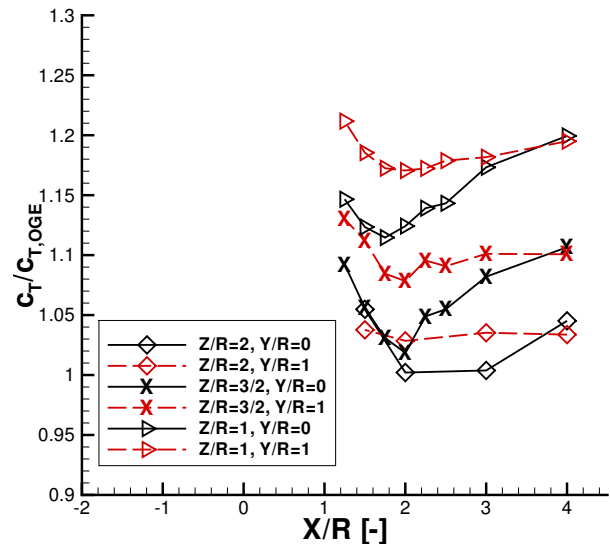
(b) Ratio of thrust coefficient c_T to thrust coefficient OGE, $Z/R = 1, 3/2, 2$
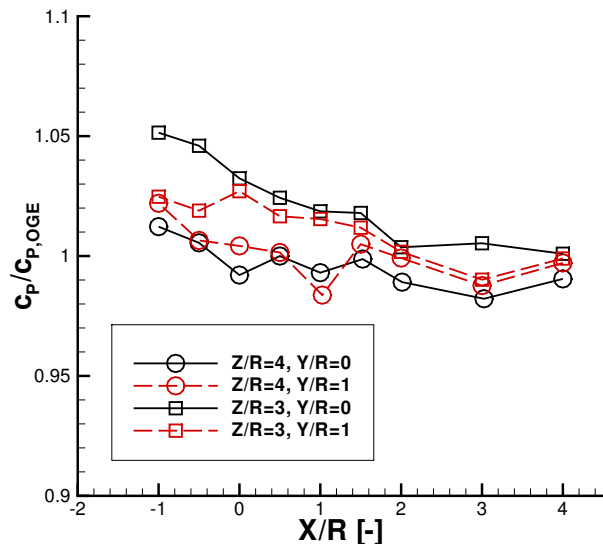
(c) Ratio of power coefficient c_P to power coefficient OGE, $Z/R = 3, 4$
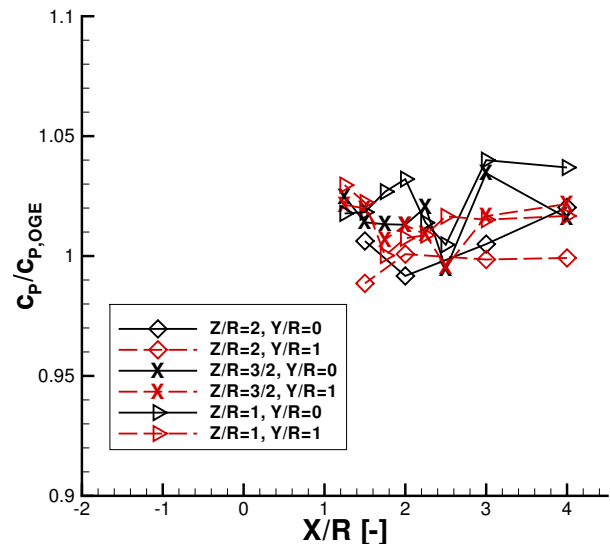
(d) Ratio of power coefficient c_P to power coefficient OGE, $Z/R = 1, 3/2, 2$

Fig. 6: Thrust and power coefficient as function of rotor position, at different rotor heights
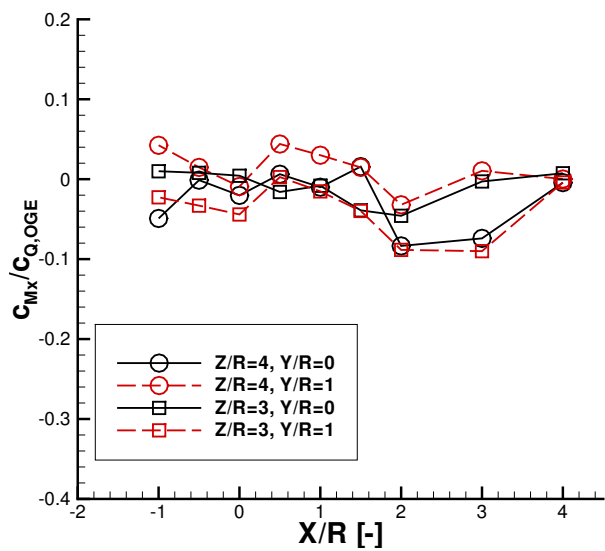
(a) Ratio of $x-$moment coeff. to OGE torque co-eff., $Z/R = 3, 4$
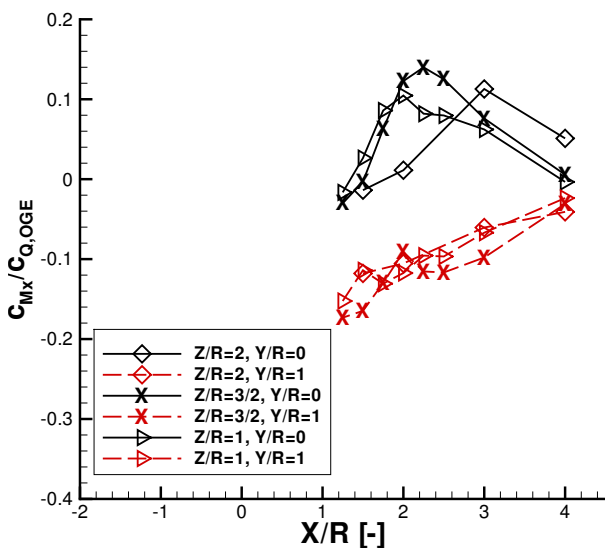
(b) Ratio of $x-$moment coeff. to OGE torque co-eff., $Z/R = 1, 3/2, 2$
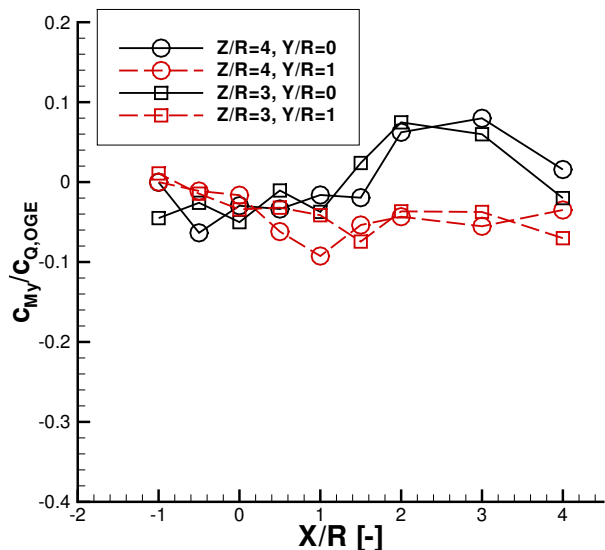
(c) Ratio of $x-$moment coeff. to OGE torque co-eff., $Z/R = 3, 4$
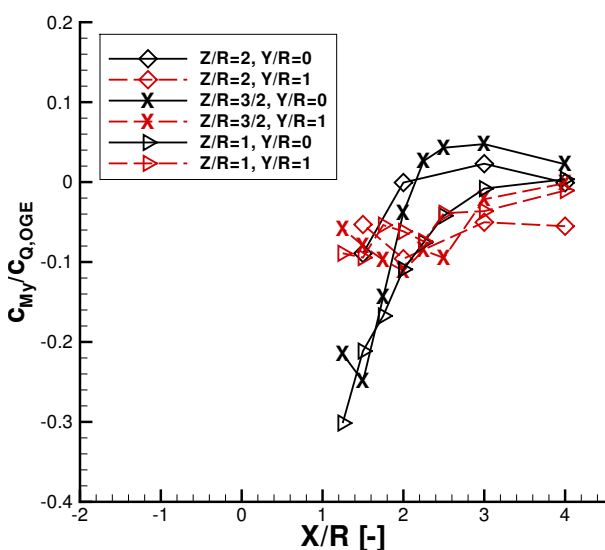
(d) Ratio of $x-$ moment coeff. to OGE torque coeff., $Z/R = 1, 3/2, 2$

Fig. 7: x and y moment coefficients as function of rotor position, at different rotor heights
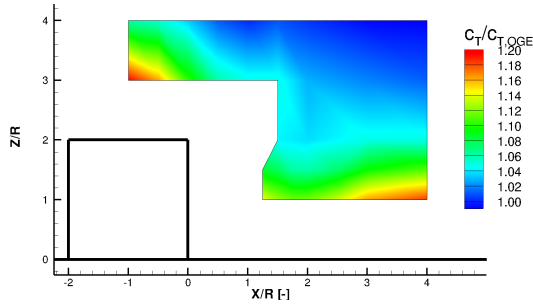
(a) Ratio of thrust coefficient c_T to thrust coefficient OGE, $Y/R = 0$
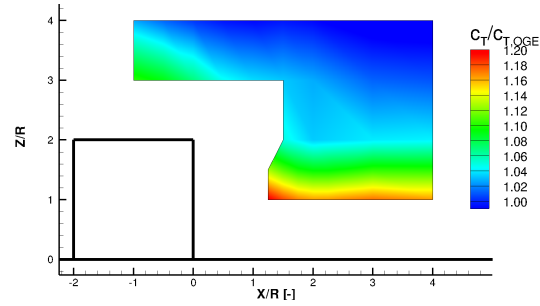
(b) Ratio of thrust coefficient c_T to thrust coefficient OGE, $Y/R = 1$
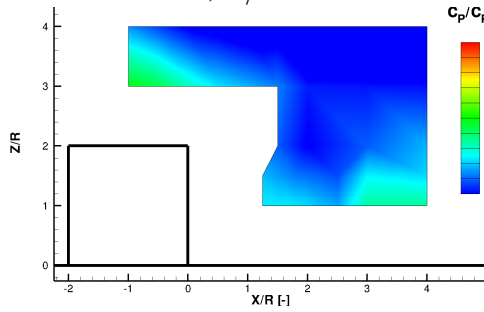
(c) Ratio of power coefficient c_P to power coefficient OGE, $Y/R = 0$
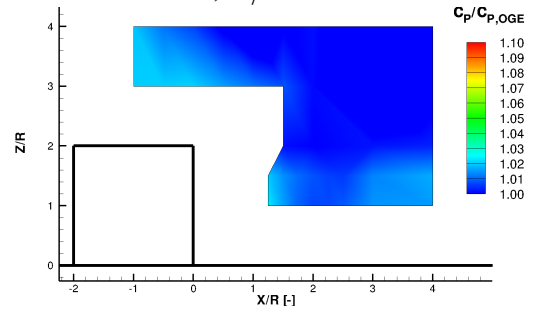
(d) Ratio of power coefficient c_P to power coefficient OGE, $Y/R = 1$
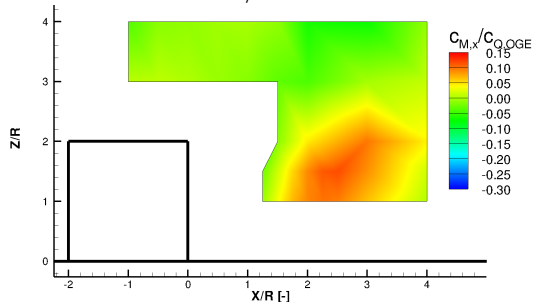
(e) Ratio of x−moment coeff. to OGE torque coeff., $Y/R = 0$
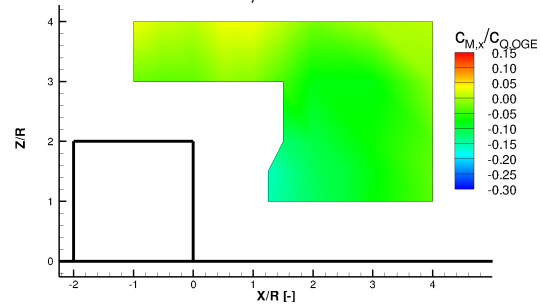
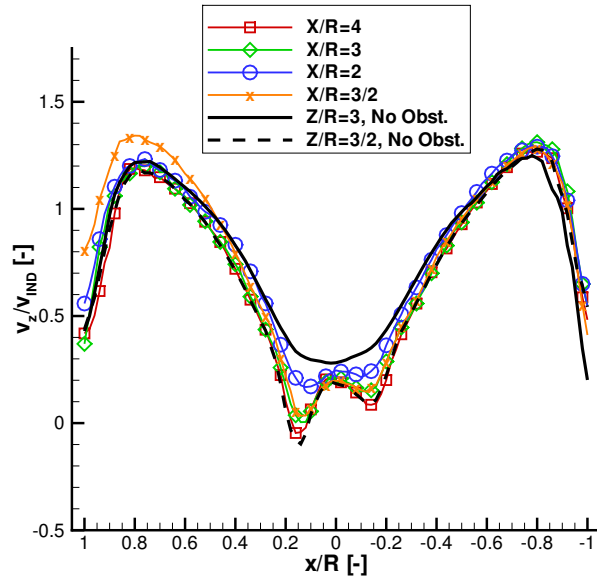(f) Ratio of x−moment coeff. to OGE torque coeff., $Y/R = 1$
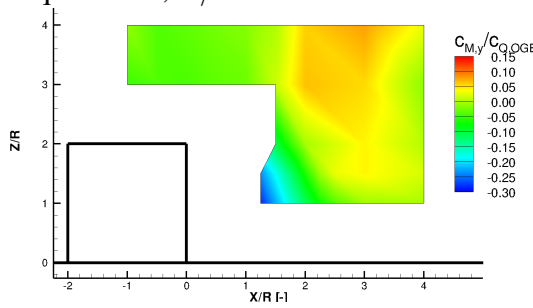
(g) Ratio of y−moment coeff. to OGE torque coeff., $Y/R = 0$
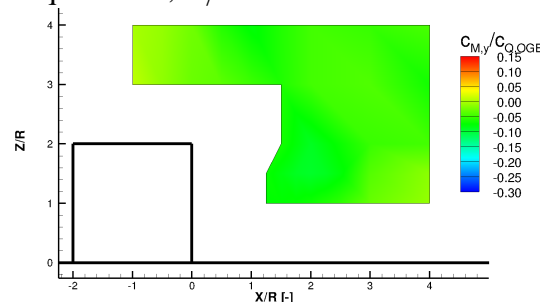
(h) Ratio of y−moment coeff. to OGE torque coeff., $Y/R = 1$

Fig. 8: Contours of the loads acting on the rotor as function of rotor position. Rotor placed at $Y/R = 0$, left, and at $Y/R = 1$, right.
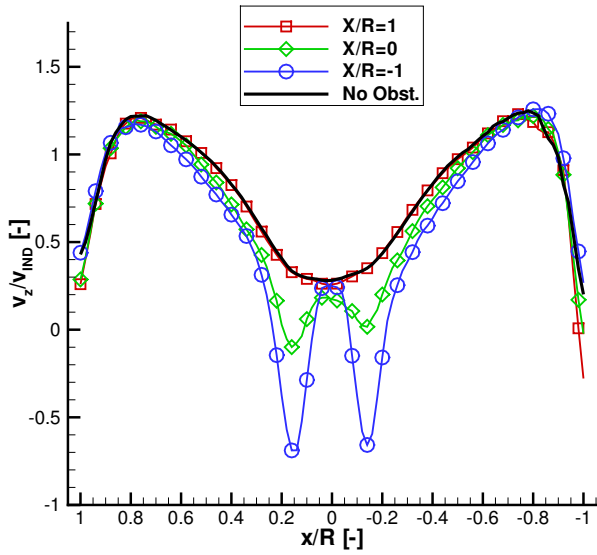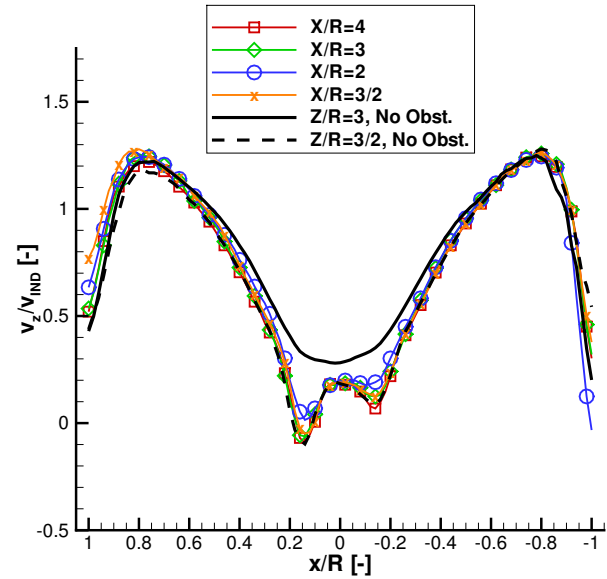
(a) $Z/R = 3, Y/R = 0$
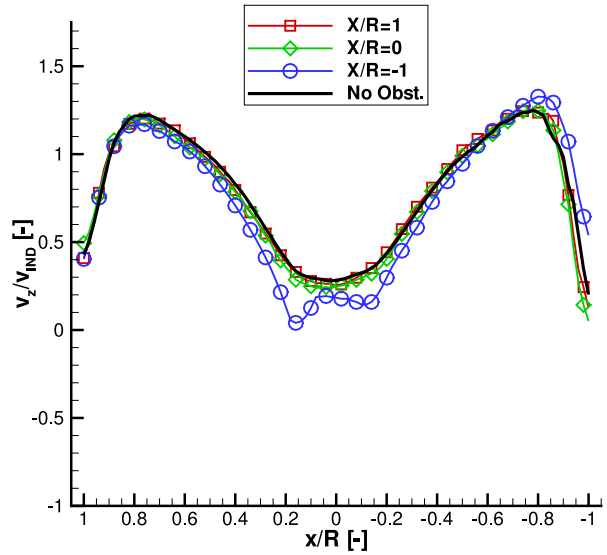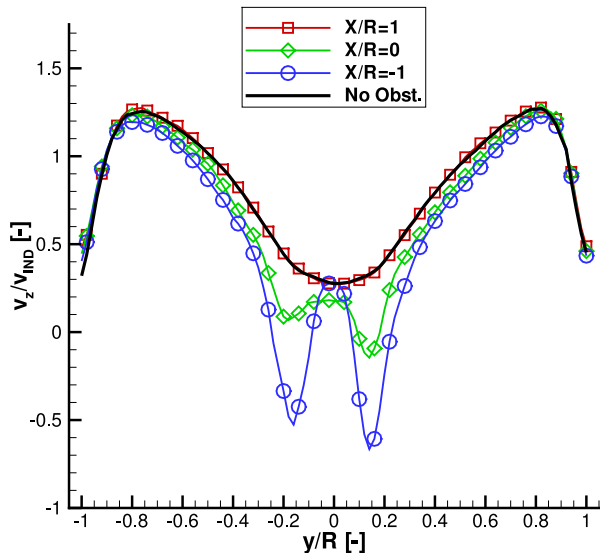
(b) $Z/R = 3, Y/R = 1$

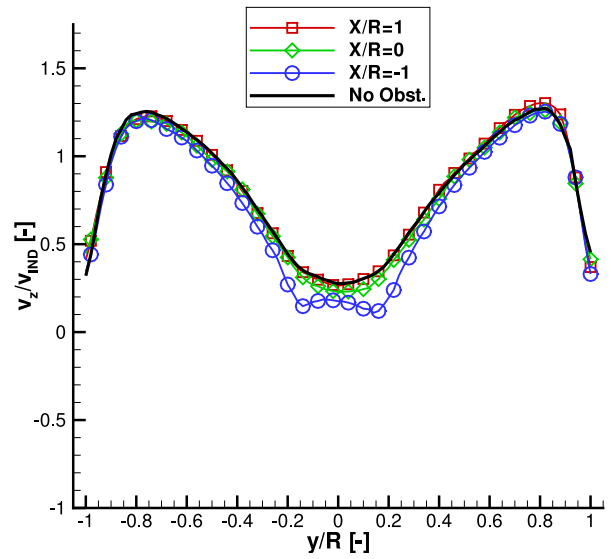(c) $Z/R = 3/2, Y/R = 0$. The obstacle is on the left of the plot.

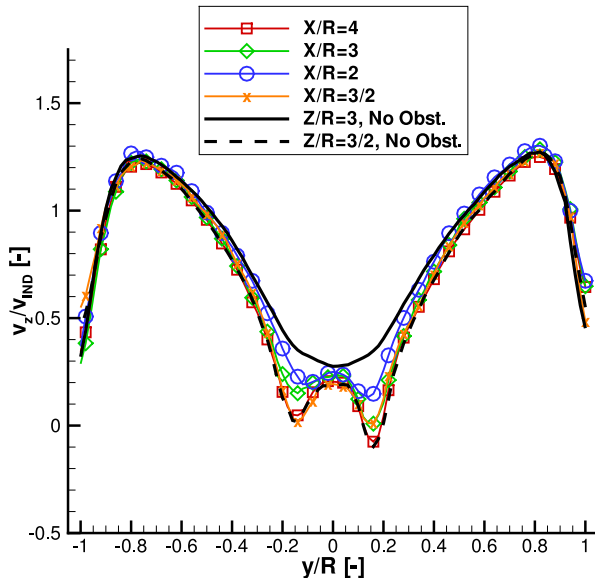(d) $Z/R = 3/2, Y/R = 1$. The obstacle is on the left of the plot.

Fig. 9: LDA Measurement of the induced velocity, x-sweep. Rotor placed at $Y/R = 0$, left, and at $Y/R = 1$, right. Velocities are scaled by the hover induced velocity V_{IND}.
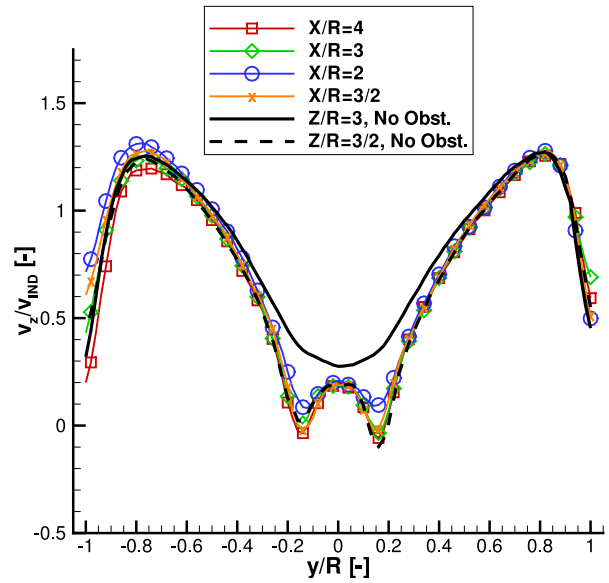
(a) $Z/R = 3, Y/R = 0$

(b) $Z/R = 3, Y/R = 1$

(c) $Z/R = 3/2, Y/R = 0$. The obstacle is on the left of the plot.

(d) $Z/R = 3/2, Y/R = 1$. The obstacle is on the left of the plot.

Fig. 10: LDA Measurement of the induced velocity, y-sweep. Rotor placed at $Y/R = 0$, left, and at $Y/R = 1$, right. Velocities are scaled by the hover induced velocity V_{IND}.

(a) $X/R=3/2$, $Y/R=0$, $Z/R=1$ (b) $X/R=3/2$, $Y/R=0$, $Z/R=3/2$ (c) $X/R=3/2$, $Y/R=0$, $Z/R=2$

(d) $X/R=2$, $Y/R=0$, $Z/R=1$ (e) $X/R=2$, $Y/R=0$, $Z/R=3/2$ (f) $X/R=2$, $Y/R=0$, $Z/R=2$

(g) $X/R=3$, $Y/R=0$, $Z/R=1$ (h) $X/R=3$, $Y/R=0$, $Z/R=3/2$ (i) $X/R=3$, $Y/R=0$, $Z/R=2$
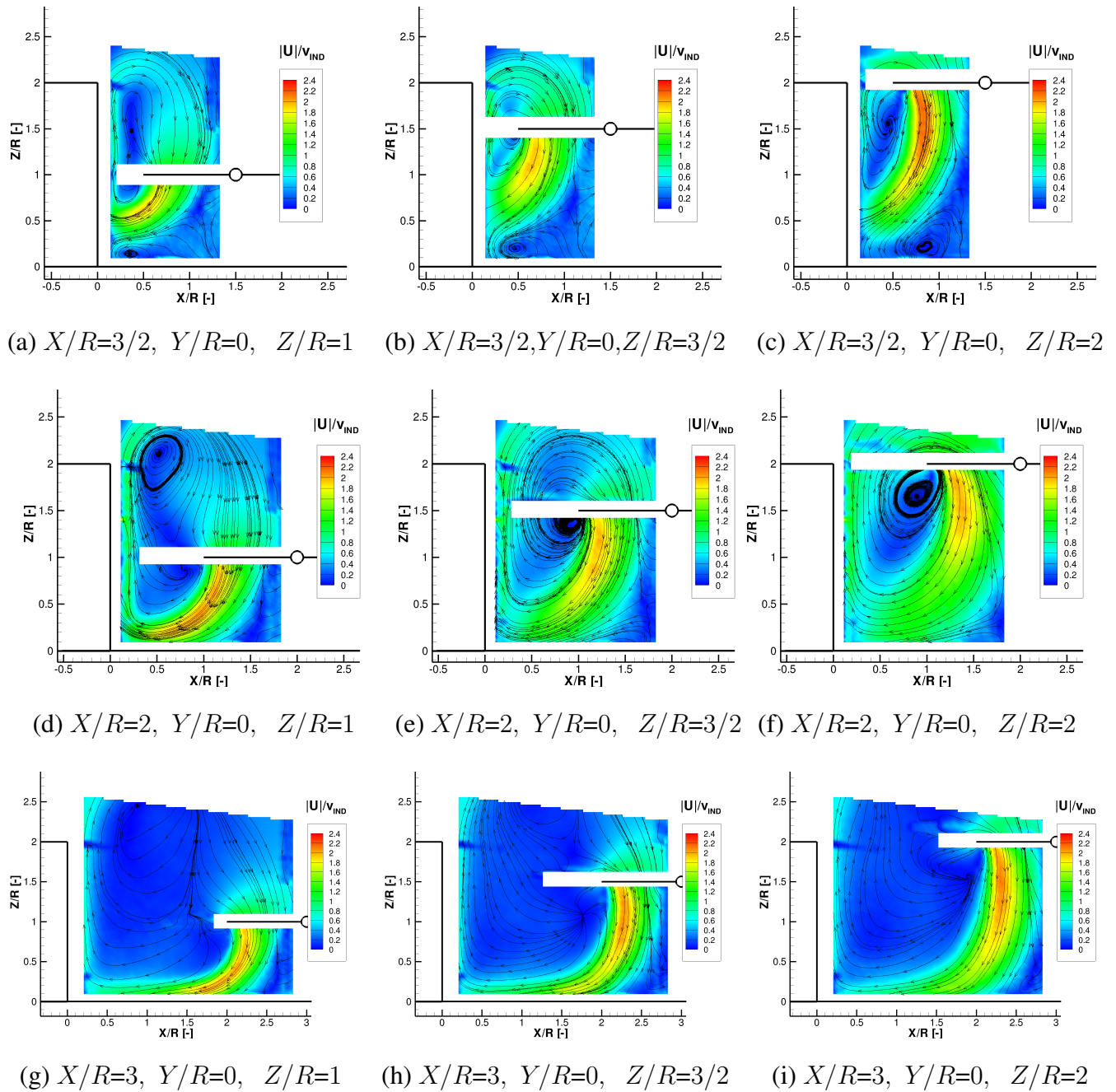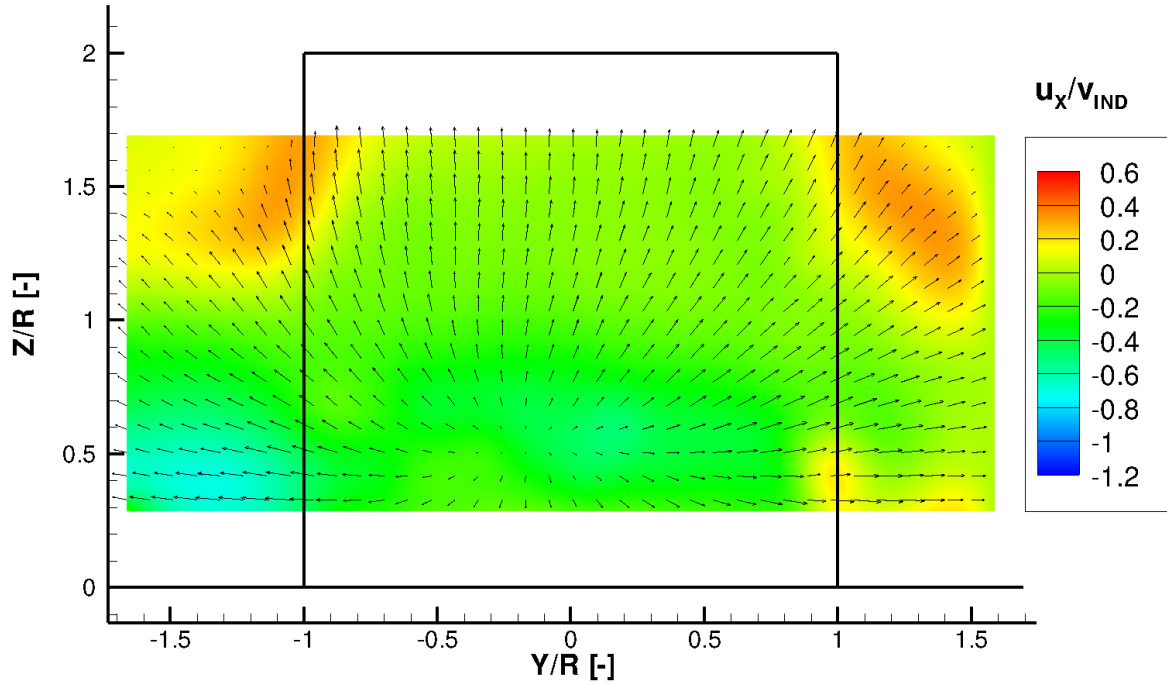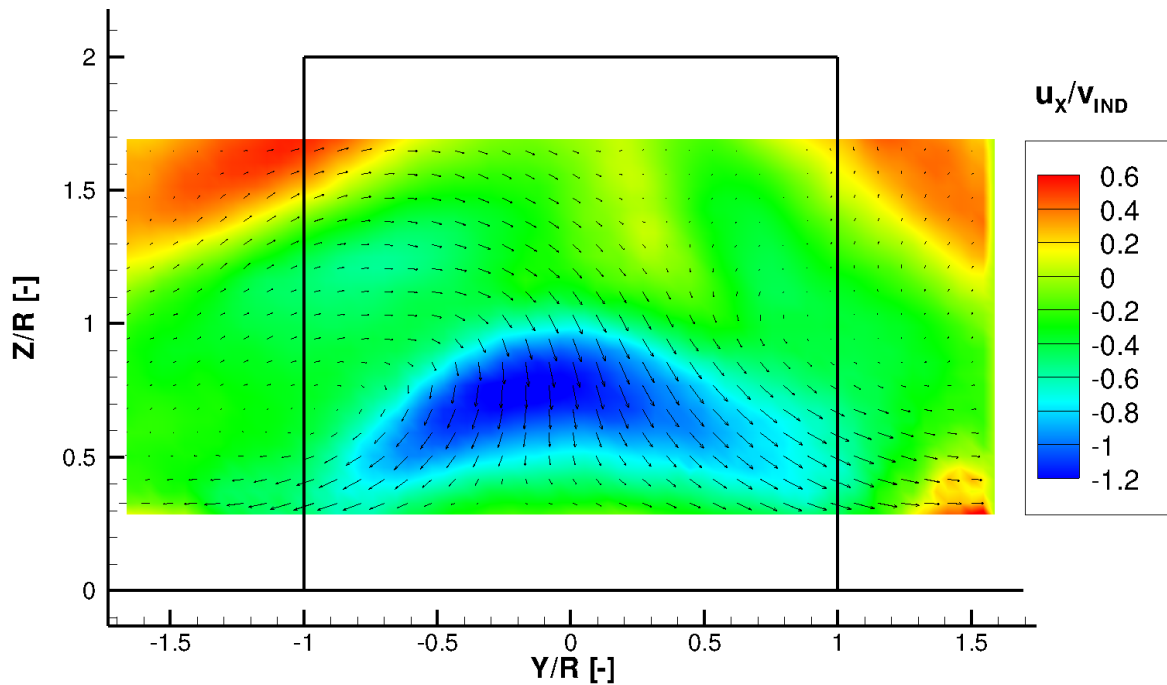
Fig. 11: PIV Measurements. In-plane velocity magnitude contours and in-plane streamlines in the symmetry plane ($Y/R = 0$) for different rotor positions. Velocities are scaled by the hover induced velocity V_{IND}.

(a) Transverse measurement plane at $X/R = 0.1$

(b) Transverse measurement plane at $X/R = 0.466$

Fig. 12: Out-of-plane velocity contours and in-plane velocity vectors. Rotor Placed at $X/R = 3/2$, $Y/R = 0$, $Z/R = 2$. A negative out-of-plane velocity points towards the obstacle. Velocities are scaled by the hover induced velocity V_{IND}.
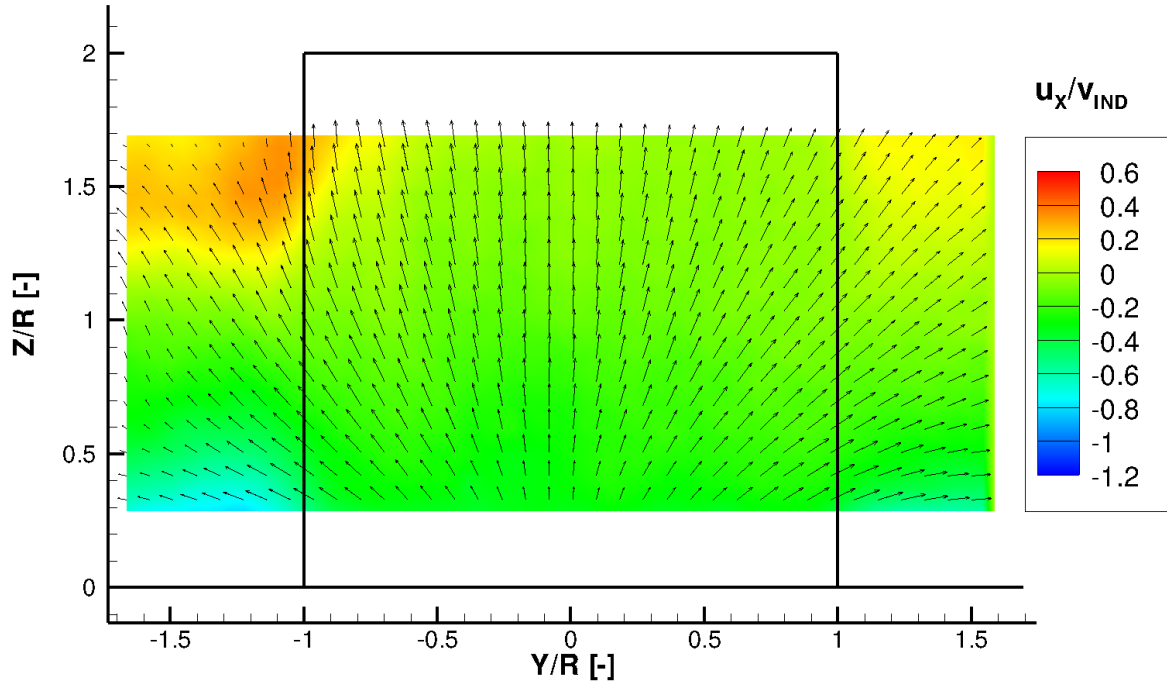
(a) Transverse measurement plane at $X/R = 0.1$

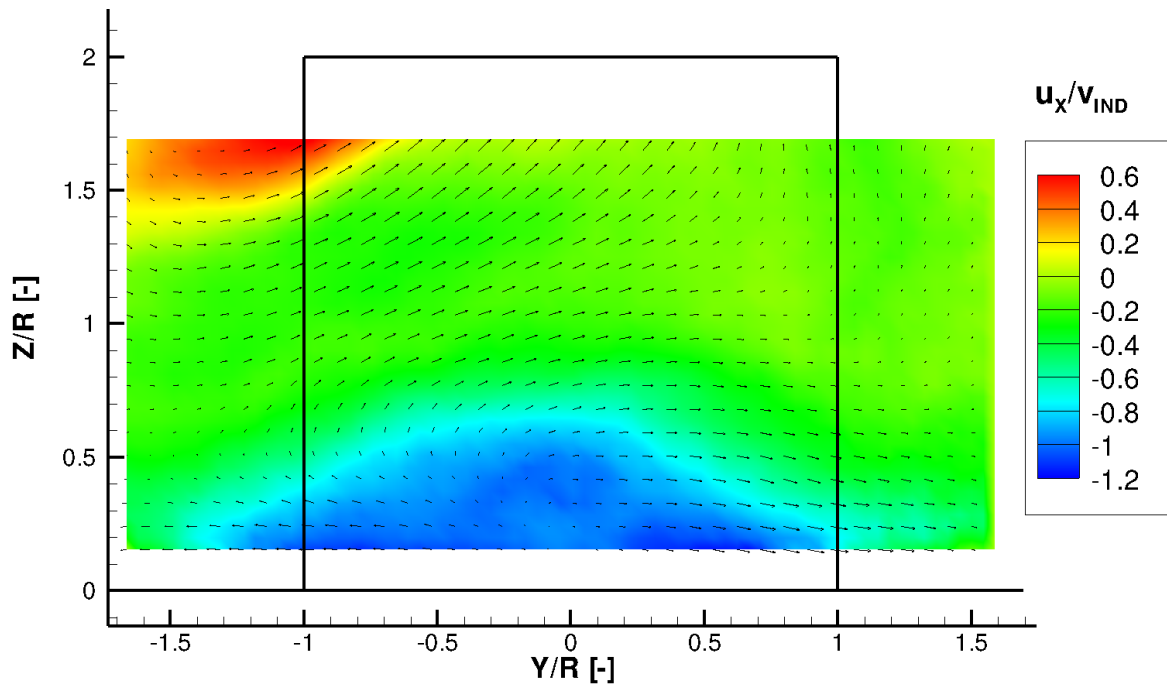(b) Transverse measurement plane at $X/R = 0.466$

Fig. 13: Out-of-plane velocity contours and in-plane velocity vectors. Rotor Placed at $X/R = 2, Y/R = 0, Z/R = 2$. A negative out-of-plane velocity points towards the obstacle. Velocities are scaled by the hover induced velocity V_{IND}.

Table 1: Main features and operational conditions of the Rotor Rigs

Characteristics	Symbol	Large rotor rig	Small rotor rig
Cubic Obstacle size	L	1 m	0.3 m
Rotor diameter	D	1 m	0.3 m
Number of blades	N_b	4	2
Blade chord	c	53 mm	31.7 mm
Solidity	σ	0.135	0.134
Blade geometry		Untapered, untwisted	Untapered, untwisted
Collective pitch	θ_c	8°	8°
Rotor rotational frequency	Ω	1200 RPM (20 Hz)	4000 RPM (66.6 Hz)
Rotor rotational direction		clockwise	clockwise
Reynolds Number at blade tip	Re_{TIP}	220000	132000
Mach Number at blade tip	M_{TIP}	0.18	0.18
OGE Thrust coefficient	$c_{T,OGE}$	$7.36 \cdot 10^{-3}$	$6 \cdot 10^{-3}$
Type of Experimental investigation		Load measurement Inflow LDA measurements	Stereo-PIV

Table 2: Out-of-Ground-Effect (OGE) reference condition

$c_{T,\mathbf{OGE}}$	$7.36 \cdot 10^{-3}$
$c_{Q,\mathbf{OGE}}, c_{P,\mathbf{OGE}}$	$8.75 \cdot 10^{-4}$
$FM_{\mathbf{OGE}}$	0.51